DIRECT NUMERICAL SIMULATION OF H-TYPE TRANSITION IN A FLAT-PLATE BOUNDARY LAYER WITH SUPERCRITICAL FLUIDS

P. C. Boldini[1], R. Gaspar[2], B. Bugeat[1], P. Costa[1], J. W. R. Peeters[1] and R. Pecnik[1]

[1] *Delft University of Technology, Process & Energy Department, the Netherlands*

[2] *University of Liège, Department of Aerospace and Mechanical Engineering, Belgium*

p.c.boldini@tudelft.nl, r.pecnik@tudelft.nl

Abstract

We investigate the laminar-to-turbulent transition of highly non-ideal supercritical fluids. The controlled H-type breakdown in a three-dimensional flat-plate boundary layer is chosen. Direct numerical simulations are performed at low Mach numbers, for isothermal and heated walls. We consider a fluid following the Van der Waals (VdW) equation of state (EoS) at a supercritical reduced pressure of $p_r = 1.10$. A newly developed GPU-accelerated code is first successfully validated against linear two-dimensional simulations using the VdW EoS, and transitional simulations using ideal gas. Subsequently, H-type breakdown of two subcritical (liquid-like only) and one strongly-stratified transcritical (pseudo-boiling) profiles are considered. As the wall temperature approaches the Widom line, the formation of staggered Λ-vortices, with hairpin-shaped vortices at their tips, is delayed. When the wall temperature is higher than the pseudo-boiling temperature, the transition scenario differs from the classical H-type breakdown. Patterns of Λ-structures are alternated by high-low-velocity and -density streaks before hairpin-shaped vortices form. Finally, the skin friction coefficient and Stanton number are analysed, shedding light on the thermodynamic-regime dependence of the transitional overshoot.

1   Introduction

In recent years, supercritical fluids have gained interest in industrial applications to increase their efficiency; for example, in supercritical CO_2 (hereafter, sCO_2) power cycles (Liu et al. (2019)). Here, the complex, non-ideal thermodynamic mechanisms above the critical pressure and the strong property variations across the Widom line (i.e. $\max(C_p)$, see figure 1) play a key role in the flow instability and transition mechanisms.
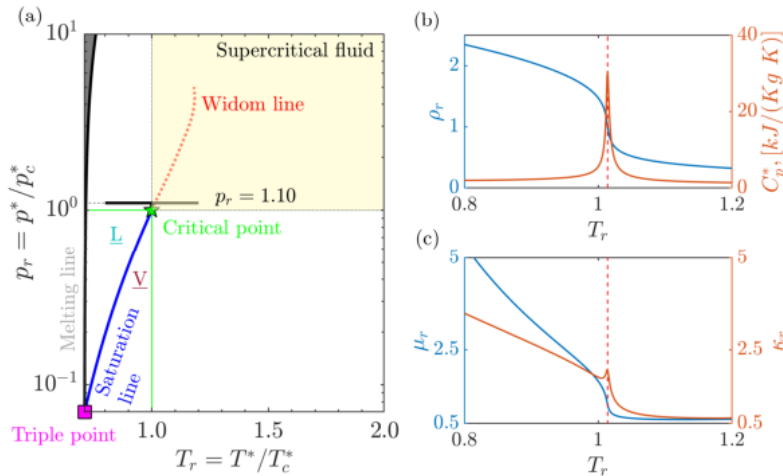

Figure 1: (a) Pressure-temperature (p–T) diagram of CO_2 along with the triple point (magenta), critical point (green), saturation line (blue), Widom line (red line) and supercritical fluid region (sCO_2) in yellow. At a reduced pressure of $p_r = 1.10$ as a function of reduced temperature T_r: (b) reduced density ρ_r and dimensional specific heat C_p^*, (c) reduced viscosity μ_r and reduced thermal conductivity κ_r. The Widom line (- - -) is at T_{pc}^*, or $T_{r,pc} = 1.024$.

In fact, the prediction of the transition location is a key aspect in order to understand how heat transfer and wall friction evolve. Yet, knowledge of how a supercritical flow transitions to turbulence is unknown; only the stability of non-ideal gases in boundary layers has been recently studied by linear stability analyses on sCO_2. A review can be found in Robinet & Gloerfelt (2019). For instance, Ren et al. (2019b) found that, in transcritical boundary layers, the flow is highly destabilised by a new inviscid mode (Mode II), which is not related to Mack's second mode. Following Ren's work but ruling out any acoustic effect (low-Mach-number approximation), Bugeat et al. (2022) carried out an inviscid stability analysis of Mode II. Its presence was confirmed, and it is associated with a general inflection point in the base flow, which in turn is generated by an extremum of the kinematic viscosity. While these studies focused on linear instabilities, the subsequent non-linear interactions towards transition to turbulence remain unexplored for supercritical fluids. On the contrary, in ideal gases, "controlled" experiments on the H-type breakdown mechanism were firstly performed by Kachanov et al. (1977). The subharmonic breakdown was later theoretically formulated by Herbert (1988). Fasel et al. (1990) confirmed these experimental and

theoretical observations by performing Direct Numerical Simulations (DNS). A more recent study was undertaken by Sayadi et al. (2013). The goal of the present study is to gain insight into the H-type breakdown in supercritical fluids which has, to our best knowledge, not been studied yet.

2 Methodology

Flow conservation equations and equation of state

We consider a single-phase flow of a generalised supercritical fluid governed by the dimensionless fully compressible Navier-Stokes equations in a Cartesian coordinate system (x, y, z):

$$\left. \begin{aligned} \partial_t \rho + \nabla \cdot (\rho \mathbf{u}) &= 0, \\ \partial_t (\rho \mathbf{u}) + \nabla \cdot (\rho \mathbf{u} \otimes \mathbf{u}) + \nabla p - (Re_\delta)^{-1} \nabla \cdot \boldsymbol{\tau} &= 0, \\ \partial_t (\rho E) + \nabla \cdot ((\rho E + p)\mathbf{u}) - \nabla \cdot (\mathbf{u} \cdot \boldsymbol{\tau}) + (Re_\delta Pr_\infty Ec_\infty)^{-1} \nabla \cdot \mathbf{q} &= 0, \end{aligned} \right\} \tag{1}$$

where $\mathbf{u}$ is the velocity vector and $E = e + \mathbf{u}^2/2$ is the total energy. The viscous stress $\boldsymbol{\tau}$ and heat flux $\mathbf{q}$ are defined as

$$\boldsymbol{\tau} = \mu \left(\nabla \mathbf{u} + \nabla \mathbf{u}^T \right) + \lambda \left(\nabla \cdot \mathbf{u} \right) \mathbf{I}, \quad \lambda = \mu_b - \frac{2}{3}\mu; \quad \mathbf{q} = -\kappa \nabla T, \tag{2}$$

where μ_b is set to 0 according to Ren et al. (2019a) and $\mathbf{I}$ is the identity matrix. The above flow conservation equations have been non-dimensionalised by the following reference values: $t = t^* U_\infty^* / L^*$, $x_i = x_i^*/L^*$, $u_i = u_i^*/U_\infty^*$, $\rho = \rho^*/\rho_\infty^*$, $p = p^*/(\rho_\infty^* U_\infty^{*2})$, $T = T^*/T_\infty^*$, $E = E^*/U_\infty^{*2}$, $\mu = \mu^*/\mu_\infty^*$, $\kappa = \kappa^*/\kappa_\infty^*$, where $(\cdot)^*$ and $(\cdot)_\infty^*$ denote dimensional and free-stream quantities, respectively. Consequently, the following non-dimensional numbers are obtained: Reynolds number $Re_\delta = \rho_\infty^* u_\infty^* \delta^*/\mu_\infty^*$, Mach number $M_\infty = u_\infty^*/a_\infty^*$, Prandtl number $Pr_\infty = C_{p,\infty}^* \mu_\infty^*/\kappa_\infty^*$, and an Eckert number $Ec_\infty = u_\infty^{*2}/(C_{p,\infty}^* T_\infty^*)$. The length scale L^* is the local boundary-layer thickness $\delta^* = (\mu_\infty^* x_\infty^*/\rho_\infty^*/u_\infty^*)^{1/2}$. The system of equations is closed by a cubic equation of state (EoS), namely the Van der Waals (VdW) EoS in reduced form. The VdW EoS is given as

$$p_r = \frac{8T_r}{3v_r - 1} - \frac{3}{v_r^2}, \tag{3}$$

with the reduced pressure $p_r = p^*/p_c^*$, reduced temperature $T_r = T^*/T_c^*$, and reduced specific volume $v_r = 1/\rho_r = \rho_c^*/\rho^*$. Subscript $(\cdot)_c^*$ denotes values at the thermodynamic critical point. With this generalised formulation, only the ratio C_v^*/R^* (i.e., the molecular degrees of freedom) needs to be specified. In addition, the analytical models of Jossi et al. (1962) and Stiel and Thodos (1964) are used for the transport properties (e.g., $\mu = f(\rho_r, T_r)$).

The computational domain is illustrated in figure 2. The inflow is located at x_0 and the outflow at x_e. The domain height is given by y_e. In the spanwise direction ($z = [0, z_e]$), periodicity is imposed. All dimensions are scaled by the boundary-layer thickness at the domain inlet δ_0. Controlled disturbances are introduced at the wall by a blowing and suction strip located between x_1 and x_2, with $x_{mid} = 0.5(x_1 + x_2)$, as

$$v(x, y = 0, z, t) = f(x) \left[A_{\text{2-D}} \sin(\omega_{\text{2-D}} t) + A_{\text{3-D}} \sin(\omega_{\text{3-D}} t) \cos(\pm \beta z) \right], \tag{4}$$

where $A_{\text{2-D}}$ and $A_{\text{3-D}}$ are the disturbance amplitudes of the primary and oblique waves, and $\omega_{\text{2-D}}$ and $\omega_{\text{3-D}}$ are the frequencies of the primary and oblique waves, respectively. The wave function $f(x)$ is chosen in agreement with Sayadi et al. (2013), whereas the spanwise wavenumber β is calculated as $\beta = 2\pi/z_e$.
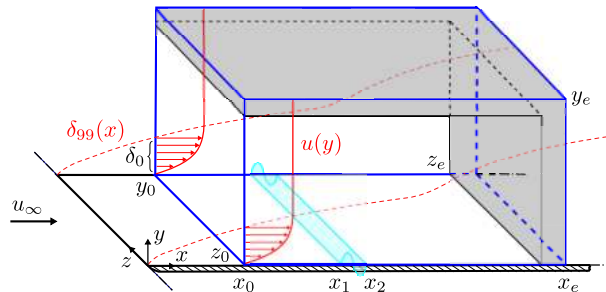

Figure 2: Computational domain in blue. In red, the velocity profile $u(y)$ and the evolution of the boundary-layer thickness $\delta_{99}(x)$. In light blue, the perturbation strip at the wall. In grey, damping zones at the boundaries.

DNS solver

In the context of DNS, the Navier-Stokes equations (equation 1) are numerically integrated with a newly developed in-house finite-difference solver, SCRINS (SuperCRItical Navier-Stokes). It is written in Modern Fortran, using MPI for parallelisation and OpenACC for GPU offloading, making it capable of running on many-GPU systems. Time integration is based on an explicit third-order Runge-Kutta scheme, whereas the spatial derivatives are

discretised using a sixth-order central finite-difference method. In order to achieve stable and non-dissipative simulations, a cubic-split form of the momentum convective terms, which was first introduced by Kennedy and Gruber (2008), is employed (see Kuya et al. (2018)). This split convective form can preserve both kinetic energy and entropy (KEEP), while minimising aliasing errors. In addition, the newly KEEP$_{PE}$ scheme of Shima et al. (2021) is included to guarantee pressure equilibrium at the discrete level.

Boundary conditions (BC) based on the local one-dimensional inviscid set of equations are chosen; for a non-ideal gas, they follow the derivation of Okong'o and Bellan (2001). Non-reflecting BCs are imposed at the inflow ($\rho = \rho_\infty$), free-stream ($p = p_\infty$), and outflow ($p = p_\infty$) planes. At the wall, the no-slip and no-penetration conditions are used, and it is isothermal ($T = T_w$). The initial condition inside the domain is given by the laminar compressible boundary-layer equations (see Ren et al. (2019b)). Additionally, damping sponge layers are applied at the boundaries in order to minimise disturbance reflections in the full viscous flow (see Franko & Lele (2013)).

Linear stability solver

Linear stability theory (LST) is used for: (1) validation of the DNS for the development of two-dimensional (2-D) waves induced by the perturbation strip (section 3), (2) preliminary analysis of the modal instabilities in the cases here studied (section 4). In agreement with Ren et al. (2019), the linearised stability equations are numerically solved by adopting the spatial framework: the spatial growth is obtained from the imaginary part of the streamwise wavenumber α. When $\alpha_i < 0$, spatial amplification occurs.

3 Validation

The aforementioned Navier-Stokes solver SCRINS has been extensively validated for various 2-D LST and three-dimensional (3-D) DNS cases with both ideal and non-ideal gas properties. Two validation cases are presented in this paper. In the first case, a DNS in the transcritical regime is compared to LST results for the linear stage using the VdW EoS. Secondly, with respect to the here considered H-type breakdown, one full transition to turbulence is performed and compared to the ideal-gas results of Herbert (1988) and Sayadi et al. (2013).

Linear stage of transition

When the DNS has reached a periodic solution, the linear infinitesimal-amplitude ($A_{2\text{-}D} = 10^{-7}$) disturbance evolution is extracted. Then, the results are Fourier transformed in time with the fundamental circular frequency $\Omega = \omega_{2\text{-}D}/2$ ($\omega_{3\text{-}D} = 0$); 50 samples are taken within two forcing periods. The growth rate $-\alpha_i(x)$ of the fundamental mode is consequently calculated (see Ren et al. (2019b)) and displayed in figure 3(a). The flow parameters are: $M_\infty = 0.39$, $Ec_\infty = 0.05$, $T_{r,\infty} = 0.92$, $p_r = 1.10$, and $Pr_\infty = 3.15$. This setup corresponds to sCO$_2$ at $T_\infty^* = 280$ K (liquid-like free stream), while the wall temperature is instead $T_{r,w} = 1.03$ (gas-like). This flow case belongs to the transcritical regime at supercritical pressure. At these conditions, the only modal instability present in the flow is caused by Mode II. Here, a dimensionless frequency of $F_{2\text{-}D} = \omega_{2\text{-}D}/Re_\delta = 50 \times 10^{-6}$ is selected.

Non-linear stage of transition

A "classical" subharmonic breakdown is simulated and compared to the theoretical results of Herbert (1987) and the numerical results of Sayadi et al. (2013) for ideal gas. The Mach number is set to $M_\infty = 0.2$, the free-stream temperature to $T_\infty^* = 300$ K, and the wall is assumed to be adiabatic. The dimensions of the computational domain are $1 \leq x/\delta_0 \leq 400$ in the streamwise direction, $0 \leq y/\delta_0 \leq 20$ in the wall-normal direction and $0 \leq z/\delta_0 \leq 9.63$ in the periodic spanwise direction. The inlet boundary-layer thickness is based on the inlet Reynolds number of $Re_{\delta,0} = \sqrt{10^5}$. The disturbance strip begins at $x_1/\delta_0 = 41.8$ and ends at $x_1/\delta_0 = 51.8$. It induces a Tollmien-Schlichting (TS) wave ($A_{2\text{-}D} = 1.75 \times 10^{-3}$) at a reduced frequency of $F_{2\text{-}D} = 124 \times 10^{-6}$ and a pair of oblique waves ($A_{3\text{-}D} = 2.5 \times 10^{-5}$ with $\beta = \pm 0.65$) with $F_{3\text{-}D} = 62 \times 10^{-6}$. Grid resolutions are $\Delta x/\delta_0 = 0.09$ and $\Delta z/\delta_0 = 0.08$; at $Re_\delta = 700$, they are equal in viscous units to $\Delta x^+ = 5.7$ and $\Delta z^+ = 5.1$ with $y_{min}^+ = 0.63$.
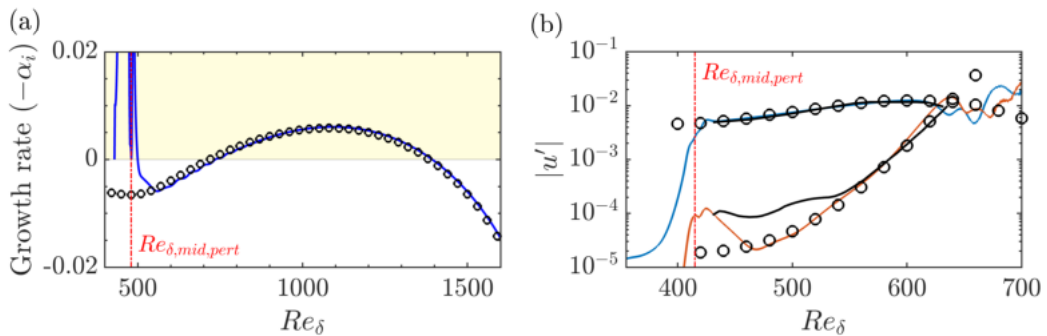

Figure 3: (a) comparison between DNS and LST: growth rate for DNS (——) and LST (○). (b) downstream development of the $|u'|$-disturbance amplitude at constant $y/\delta_0 = 0.26$: mode (1,0), —— ; (1/2,1), —— ; ○, Herbert (1988); ——, Sayadi et al. (2013). The location of the disturbance strip is reported with a dash-dotted line (–·–).

Figure 3(a) displays the evolution of the growth rate as a function of the local Reynolds number Re_δ for the

DNS simulation and LST. Overall, the DNS shows good qualitative agreement with LST. Yet, a small quantitative shift is observed due to non-parallel effects. Figure 3(b) shows the spatial development of the Fourier transformed streamwise velocity disturbance $|u'|$ in the range $Re_\delta = [350, 700]$. Here, (h, k) indicates a wave with frequency $h \cdot F$ and spanwise wavenumber $k \cdot \beta$. Good quantitative agreement between the current DNS results, theory, and literature is observed both for the primary and secondary modes.

4   Results

All simulations are conducted at the same supercritical pressure of $p_r = 1.10$, free-stream temperature of $T_{r,\infty} = 0.90$ (liquid-like region), and a finite Mach number of $M_\infty = 0.2$. Three different reduced wall temperatures are used (two in the liquid-like region and one in the gas-like region); see table 1.

EoS	p_r	$T_{r,pc}$	$T_{r,\infty}$	$T_{r,0}$	M_∞	Ec_∞	Pr_∞	C_v^*/R^*	$T_{r,w}$	T_w^*/T_∞^*	Case	Regime
									0.90	1.0	Tw090	Subcritical
VdW	1.10	1.024	0.90	0.924	0.2	0.016	1.0	9/2	0.95	1.056	Tw095	Subcritical
									1.10	1.222	Tw110	Transcritical

Table 1: Base-flow properties of the cases under consideration. $T_{r,w}$ stands for the reduced wall temperature. For the transcritical case (Tw110), the temperature profile crosses the Widom line (i.e., $T_{r,w} > T_{r,pc}$). The reduced total temperature $T_{r,0}$ is calculated according to Nederstigt & Pecnik (2023).

In figure 4, laminar boundary-layer profiles are displayed for the three cases listed in table 1. The strongest density variation (figure 4(c)) can be found in the transcritical case.
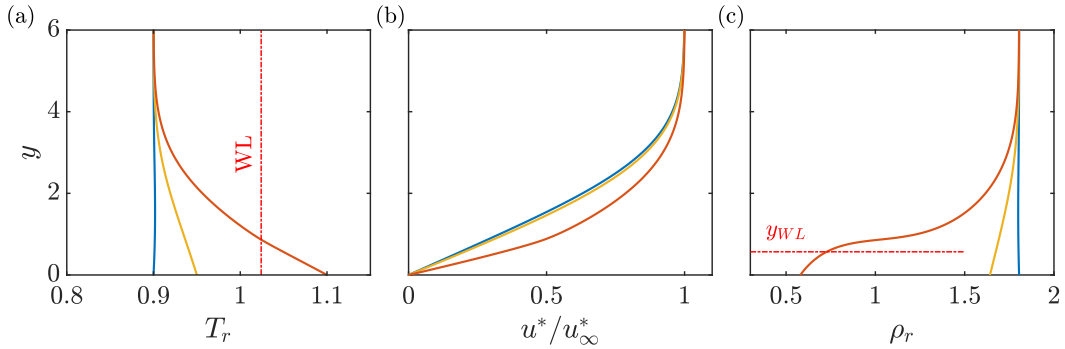

Figure 4: Self-similar base-flow profiles: (a) reduced temperature, (b) non-dimensional streamwise velocity, and (c) reduced density. $T_{r,w} = 0.90$ (——), $T_{r,w} = 0.95$ (——), and $T_{r,w} = 1.10$ (——). In (a), the Widom line (WL) is marked with a dash-dotted line (-·-). In (c), the y-location of the WL is displayed by a horizontal dash-dotted line (-·-).

Using these profiles, a linear stability analysis is performed. Their stability diagrams are compared in figure 5, in which the growth rate $(-\alpha_i)$ is plotted in the Reynolds number Re_δ – dimensionless frequency F space. Here, neutral stability for a corresponding ideal-gas case is indicated with a dotted blue line. Wall heating is found to stabilise the TS wave in the subcritical regime. In the transcritical regime, two modal instabilities appear (Mode I and II), consistent with Ren et al. (2019). Here, Mode I (TS-wave like), non-monotonic across the Widom line, is moderately unstable, whereas inviscid Mode II is highly unstable.
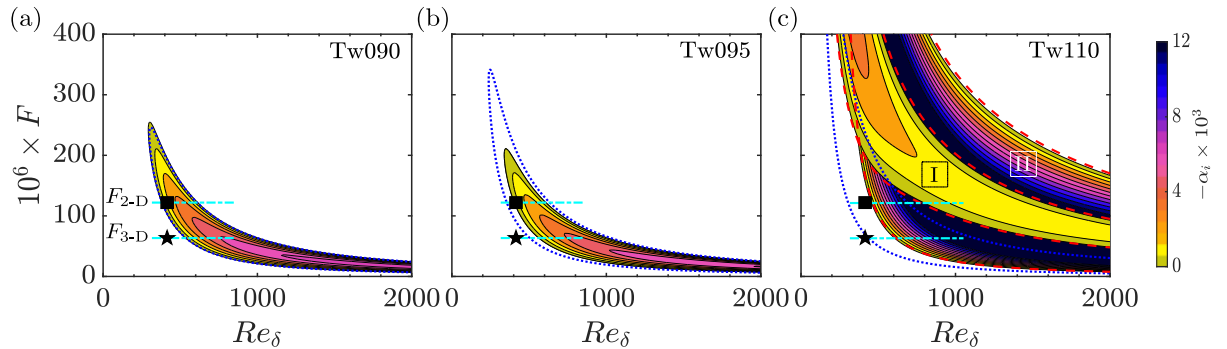

Figure 5: LST of the subcritical and transcritical VdW cases: stability diagrams for the three different wall temperatures. Neutral stability curve for ideal gas (-·-) and for VdW at $M_\infty = 0$ (– – –). The extent of the DNS domain (-·-), and the location of the disturbance strip (2-D wave ■, 3-D waves ★) and associated frequencies are indicated.

Mimicking the the ideal-gas case of Sayadi et al. (2013), the DNS cases have been selected such that a modal instability is triggered at the same primary frequency $F_{2\text{-D}}$. Therefore, in a disturbance strip at $Re_{\delta,mid} = 415$, the two-dimensional wave $(1,0)$ with $F_{2\text{-D}} = 124 \times 10^{-6}$, $A_{2\text{-D}} = 1.75 \times 10^{-3}$ and oblique subharmonic waves $(1, \pm 1)$ with $F_{3\text{-D}} = 0.5 F_{2\text{-D}}$, $A_{3\text{-D}} = 2.5 \times 10^{-5}$ are introduced. From figure 5, it can be noticed that in the trans-

critical regime the primary instability is mainly caused by Mode II, and not by a TS-wave like instability. Further computational details are given in table 2.

Case	L_x/δ_0	L_y/δ_0	L_z/δ_0	N_x	N_y	N_z	Δx^+	Δy^+_{min}	Δz^+	$Re_{\theta,max}$
Tw090	400	20	9.63	6550	400	150	4.5	0.53	4.7	564
Tw095	400	20	9.63	6550	400	150	4.9	0.58	5.1	556
Tw110	668	40	9.63	10240	700	160	5.4	0.46	4.9	586

Table 2: Numerical parameters of the H-type simulations. Viscous units $(\cdot)^+$ are calculated at $Re_{\theta,max}$.

Snapshots of the streamwise velocity inside the boundary layer (xz-plane) at a constant wall-normal height of $y/\delta_0 = 0.35$ are presented in figure 6. The staggered alignment of Λ-vortices is noticeable in figure 6(a)-(b) for the subcritical cases. Farther downstream, the Λ-structures elongate in the tip region, where they develop into a hairpin-like structure, while lifting up. An increase of wall temperature towards the Widom line (figure 6(b)) is found to delay transition, confirming the prediction given by LST in figure 5. Additionally, in case Tw095, Λ-vortices are more elongated than in case Tw090. In figure 6(c), the breakdown scenario of case Tw110 shows significant differences with the subcritical cases. A clear staggered pattern of the Λ-structures is not present. Instead, the first appearance of two elongated legs of opposite signed streamwise vorticity ω_x is only found at $Re_x \approx 5.35 \times 10^5$ (position A). Here, the induced high-velocity regions are associated with high-density regions, which is different from the subcritical regime. Downstream at $Re_x \approx 5.55 \times 10^5$ (B), streamwise-elongated structures can be seen (high-low-speed zones with high (liquid-like)-low (gas-like) density). Even farther downstream (C), streaks evolve into Λ-structures before a hairpin-shaped eddy is similarly generated, as in cases Tw09 and Tw095. Overall, the H-type breakdown in the transcritical regime takes place over a much shorter distance.
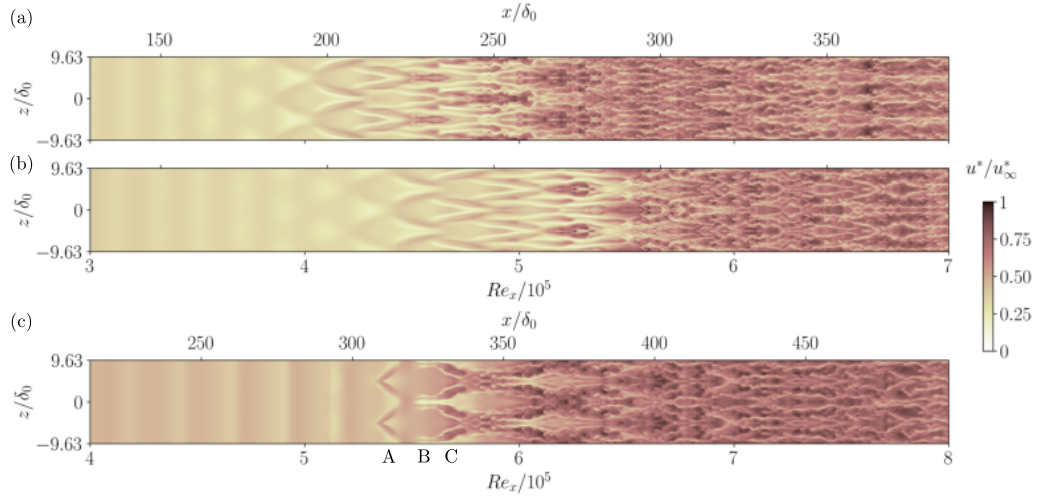

Figure 6: Contours of instantaneous streamwise velocity (xz-plane at $y/\delta_0 = 0.35$): (a) Tw090, (b) Tw095 and (c) Tw110. Spanwise domain is copied once for better visualisation. Note the different x-axis range between (a-b) and (c).

To analyse the transition mechanism, the Fourier transformed streamwise velocity disturbance is extracted from the flow field and presented as a function of the streamwise Reynolds number Re_x in figure 7. Only selected modes that take part in the early non-linear stage of the subharmonic breakdown are presented here.
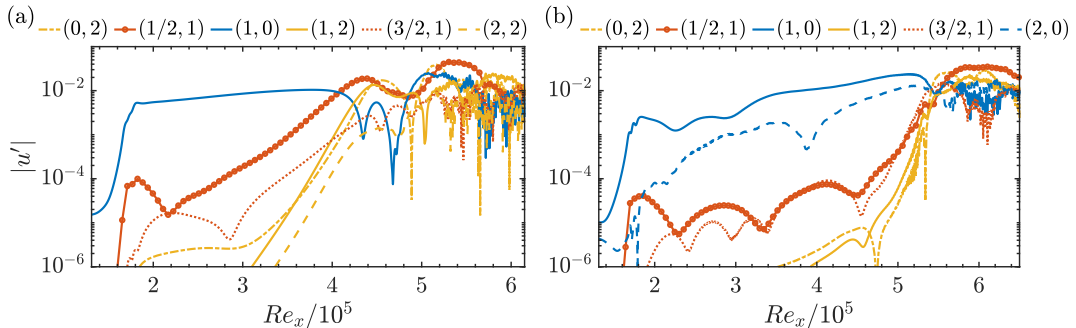

Figure 7: Streamwise development of the u' velocity extracted at $y/\delta_0 = 0.35$: (a) Tw095, (b) Tw110. The disturbance strip is located at $Re_x = 1.72 \times 10^5$

The subcritical case Tw095 in figure 7(a) shows significant resemblance to the ideal-gas case in figure 3(b). The primary 2-D mode $(1, 0)$ follows the modal growth predicted by LST in figure 5(b), whereas oblique waves $(1/2, \pm 1)$ are initially stable. Once the secondary instability occurs, mode $(1/2, 1)$ grows rapidly to finite amplitude and overtakes mode $(1, 0)$ at $Re_x \approx 4.2 \times 10^5$. This leads to the formation of the staggered Λ-structures

in figure 6(b). The non-linear generation of modes $(0,2)$, $(1,2)$, and $(2,2)$ takes place thereafter. A different behaviour of the subharmonic breakdown can be noticed for the transcritical case Tw110 in figure 7(b). Mode $(1,0)$ is initially damped at the disturbance strip in figure 5(c). Note that the second higher harmonic $(2,0)$ is unstable, and influences the other modes by non-linear interaction. The subharmonic mode $(1/2,1)$ experiences alternating growing and damping up to $Re_x \approx 4.6 \times 10^5$ before rising abruptly. Here, other modes are also strongly, non-linearly amplified. In particular, the large growth of a steady longitudinal mode $(0,2)$ has the highest amplitude at $Re_x \approx 5.5 \times 10^5$, which is the same location of the streaky structures observed in figure 6. In contrast, modes $(1/2,1)$ and $(3/2,1)$, typical of the Λ-vortices, reach their highest amplitude only after $Re_x \approx 5.8 \times 10^5$, which is also consistent with the observations made earlier for figure 6.

In order to define the transition location, the streamwise evolutions of the time- and spanwise-averaged skin friction coefficient C_f and Stanton number St are calculated. They are defined in non-dimensional form as

$$C_f = \frac{2\tau_w}{Re_\delta}, \quad St = \frac{q_w}{Re_\delta Pr_\infty Ec_\infty M_\infty^2 a_{r,\infty}^2 (h_{r,aw} - h_{r,w})}, \tag{5}$$

where $a_{r,\infty} = a_\infty^*/(p_c^* v_c^*)$ is the reduced speed of sound in the free stream, and $h_{r,aw} = h_{aw}^*/(p_c^* v_c^*)$ is the reduced the adiabatic wall enthalpy, which is equal to the total enthalpy $h_{r,0}$ for $Pr = 1$ (see flow parameters in table 1):

$$h_{r,aw} = h_{r,0} = \frac{C_{v,r} T_{r,0}}{Z_c} - \frac{3}{v_{r,0}} + p_{r,0} v_{r,0}. \tag{6}$$

The critical compressibility factor Z_c for the VdW EoS is $3/8$. In figure 8, C_f and St are presented for case Tw095 (figure 8(a)) and Tw110 (figure 8(b)). By comparing their development with u' in figure 7, the following conclusions on the wall-shear and heat-flux development can be drawn. Once the secondary instability arises, both curves very slightly deviate from their respective laminar solution. Before mode $(1/2,1)$ reaches its maximum for case Tw095 ($Re_x \approx 4 \times 10^5$) and mode $(0,2)$ reaches its maximum for case Tw110 ($Re_x \approx 4.8 \times 10^5$), the transition onset is found (i.e. $\min(C_f)$, $\min(St)$), respectively. It is followed by a steep rise as other higher modes experience strong non-linear amplification. This rise happens later for case Tw110 as the secondary instability develops farther downstream than for case Tw095. A distinct overshoot is later seen for case Tw095, representative of the H-type transition. For case Tw110, the overshoot is significantly reduced by the concurrent presence of streamwise streaks, typical of bypass transition. The Stanton number shows an analogous behaviour to the development of the skin friction coefficient for both subcritical and transcritical cases.
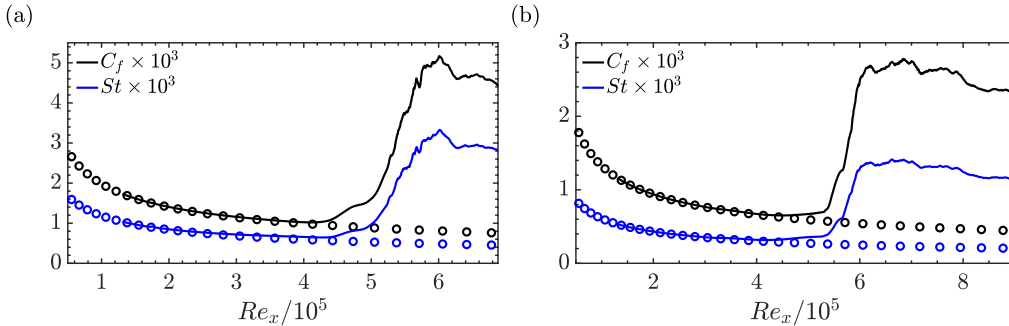

Figure 8: Time- and spanwise-averaged skin friction coefficient C_f (–) and Stanton number St (–): (a) Tw095, (b) Tw110. Solid lines are DNS results, while symbols represent the numerical integration of the self-similar laminar profile.

The boundary layer becomes turbulent at $Re_x \approx 5.6 \times 10^6$ for case Tw095. Overall, the transcritical case reveals a lower skin friction coefficient than case Tw095. In fact, despite the larger wall shear $(\partial u/\partial y)$ in the transcritical regime (see figure 4), the viscosity at the wall for the subcritical regime is a factor $\mu_w^{Tw095}/\mu_w^{Tw110} \approx 2.5$ larger. Similarly, the temperature gradient $(\partial T/\partial y)$ is larger in the transcritical case, while the thermal conductivity at the wall is smaller ($\kappa_w^{Tw110}/\kappa_w^{Tw095} \approx 0.75$).

Finally, instantaneous flow structures are displayed in figure 9 by isocontours of the Q-criterion. In the subcritical regime (figure 9(a)), the sequence of staggered Λ-structures and hairpin-shaped vortices can be clearly noticed (location A). Figure 9(b) displays the H-type transition for the transcritical case Tw110. The combination of Λ-vortices (A) and streamwise streaks (B) is noticeable. In the later transition stage, lifting of the hairpin-shaped loops is visible. From preliminary investigations of the turbulent flow statistics, it has been found that an interplay of the large vorticity structures with the influence of the Widom line enhances the fluctuations' amplitude. For instance, density fluctuations $\sqrt{\overline{\rho'\rho'}}/\bar{\rho}$ and viscosity fluctuations $\sqrt{\overline{\mu'\mu'}}/\bar{\mu}$ can reach up to 30% in the near-wall region, while they are negligible in the subcritical regime (i.e., $\approx 2\%$). Furthermore, due to the sharp gradient of C_p in the proximity of the Widom line (see figure 1), local maximal C_p-fluctuations $\sqrt{\overline{C_p'C_p'}}/\bar{C_p}$ up to 80% are found. These results confirm the investigations of Kawai (2019), in which strong property fluctuations are observed. Hence, they significantly modify the near-wall turbulence and the turbulent statistics.
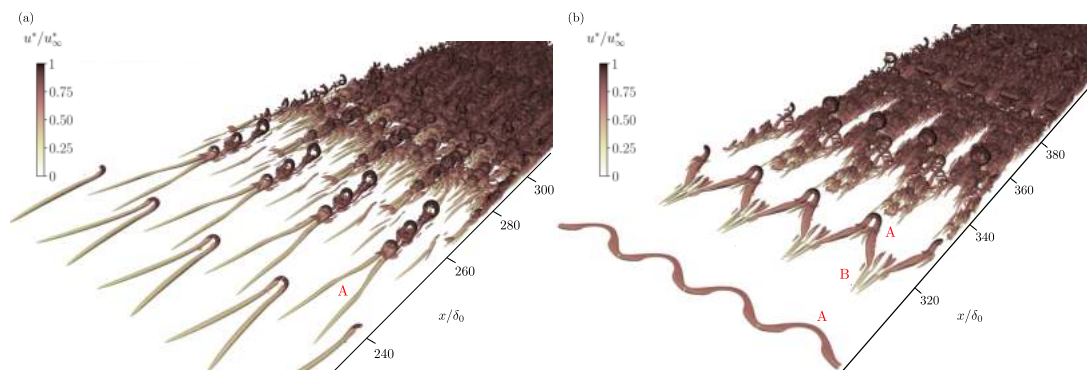
Figure 9: Visualisation of the instantaneous flow structures using isosurfaces of the Q-criterion ($Q = 0.025$), coloured by the streamwise velocity: (a) Tw095, (b) Tw110.

5   Conclusions

Direct numerical simulations were performed for the first time to study the transition to turbulence of a flat-plate boundary layer with supercritical fluids. The H-type breakdown case of Sayadi et al. (2013) at a Mach number of 0.2 was chosen as a reference scenario. After the validation of the newly developed high-order multi-GPU accelerated solver, three different flow cases were considered with respect to the pseudo-boiling temperature: two in the subcritical regime and one highly non-ideal in the transcritical regime. All share the same reduced supercritical pressure of $p_r = 1.10$ and the same free-stream conditions (e.g., $T_{r,\infty} = 0.90$), while each having a different wall temperature. The investigations highlighted that the formation of staggered Λ-vortices, followed by hairpin vortices, was delayed by a wall-temperature increase towards the Widom line. In the transcritical regime, the subharmonic instability was significantly delayed before being abruptly amplified together with other higher modes. Consequently, a combination of strong vortical structures, resembling Λ-vortices, and high-low-speed streaks with high-low-density fluid was found. In contrast to the subcritical regime with regards to the skin-friction and Stanton-number evolution, no distinct overshoot was observed. Additionally, thermophysical-property fluctuations are found to be two orders of magnitude larger than in ideal-gas simulations at the same Mach number.

Acknowledgments

References

Bugeat, B., Boldini, P. C. and Pecnik, R. (2022), On the new unstable mode in the boundary layer flow of supercritical fluids, *In Proceedings of 12th International Symposium on Turbulence and Shear Flow Phenomena (TSFP12), Osaka, Japan (Online), July 19-22.*

Fasel, H. F., Rist, U. and Konzelmann, U. (1990), Numerical investigation of the three-dimensional development in boundary-layer transition, *AIAA J.* 28, 29–37.

Franko, K. J. and Lele, S. K. (2013), Breakdown mechanisms and heat transfer overshoot in hypersonic zero pressure gradient boundary layers, *J. Fluid Mech.* 730, 491–532.

Herbert, T. (1988), Secondary instability of boundary layers, *Annu. Rev. Fluid Mech.* 20, 487–526.

Jossi, J. A., Stiel, L. I. and Thodos, G. (1962), The viscosity of pure substances in the dense gaseous and liquid phases, *AIChE Journal*, Vol. 8 (1), pp. 59–63.

Kachanov, Y. S., Kozlov, V. V. and Levchenko, V. Y. (1977), Nonlinear development of a wave in a boundary layer, *Fluid Dyn.* 12, 383–390.

Kawai, S. (2019), Heated transcritical and unheated non-transcritical turbulent boundary layers at supercritical pressures, *J. Fluid Mech.*, 865, 563–601.

Kennedy, C. A., Gruber, A. (2008), Reduced aliasing formulations of the convective terms within the Navier–Stokes equations for a compressible fluid, *J. Comput. Phys.* 227, 1676–1700.

Kuya, Y., Totani, K. and Kawai, S. (2018), Kinetic energy and entropy preserving schemes for compressible flows by split convective forms, *J. Comput. Phys.*, Vol. 375, pp. 823–853.

Liu, Y., Wang, Y. and Huang, D. (2019), Supercritical CO2 Brayton cycle: A state-of-the-art review, *Energy*, Vol. 189, 115900.

Nederstigt, P., Pecnik, R. (2023), Generalised Isentropic Relations in Thermodynamics, *Energies 2023*, 16, 2281.

Okong'o, N. and Bellan, J. (2002), Consistent boundary conditions for multicomponent real gas mixtures based on characteristic waves, *J. Comput. Phys*, 176 (2), 330–344.

Ren, J., Fu, S. and Pecnik, R. (2019a), Linear instability of Poiseuille flows with highly non-ideal fluids, *J. Fluid Mech.*, Vol. 859, 89–125.

Ren, J., Marxen, O. and Pecnik, R. (2019b), Boundary-layer stability of supercritical fluids in the vicinity of the Widom line. *J. Fluid Mech.*, Vol. 871, pp. 831–864.

Robinet, J.-C. and Gloerfelt, X. (2019), Instabilities in non-ideal fluids. *J. Fluid Mech.*, Vol. 880, pp. 1–4.

Sayadi, T., Hamman, C. and Moin, P. (2013), Direct numerical simulation of complete H-type and K-type transitions with implications for the dynamics of turbulent boundary layers, *J. Fluid Mech.*, Vol. 724, pp. 480–509.

Shima, N., Kuya, Y., Tamaki, Y. and Kawai, S. (2021), Preventing spurious pressure oscillations in split convective form discretization for compressible flows, *J. Comput. Phys.*, 427, 110060.

Stiel, L. I. and Thodos, G. (1964), The thermal conductivity of nonpolar substances in the dense gaseous and liquid regions. *AIChE Journal*, Vol. 10 (1), pp. 26–30.